



Third Epoch HST Imaging of a Nonradiative Shock in the Cygnus Loop Supernova Remnant

Ravi Sankrit¹ , William P. Blair² , and John C. Raymond³ ¹ Space Telescope Science Institute, 3700 San Martin Dr., Baltimore MD 21218, USA; rsankrit@stsci.edu² The William H. Miller III Department of Physics and Astronomy, Johns Hopkins University, 3400 N. Charles Street, Baltimore, MD, 21218, USA; wblair@jhu.edu³ Harvard-Smithsonian Center for Astrophysics, 60 Garden Street, Cambridge, MA, 02138, USA; raymond@cfa.harvard.edu

Received 2023 March 1; revised 2023 March 27; accepted 2023 March 27; published 2023 May 11

Abstract

We present new HST/WFC3 optical images of a region in the northeastern part of the Cygnus Loop supernova remnant, which includes a well-studied Balmer-line filament. These data represent the third epoch of HST H α imaging and a second epoch of [O III] λ 5007 imaging of that particular filament. The H α images were used to measure the proper motions at various locations along the shock front, and the values ranged from 55 to 85 mas yr⁻¹ with a median value of 70 mas yr⁻¹, which corresponds to a shock velocity of 240 km s⁻¹. The proper motions between epochs 1 and 2 were the same as between epochs 2 and 3, implying that there has been no measurable deceleration of the shock in the 22 yr period between the first and third epochs. The range of proper motions (and therefore shock velocities) along the filament indicate variations of over a factor of two in the preshock density. The [O III] emission is prominent toward one end of the filament where the shock has transitioned from nonradiative to radiative. The proper motion is smaller than for the H α filaments, and it corresponds to a shock velocity of about 155 km s⁻¹. The images obtained about 18 yr apart show that the [O III] morphology has not changed, which places limits on any short-timescale variations due to catastrophic cooling or thermal instabilities. We find that the effective shock age is less than the eddy turnover timescale, which implies that turbulence has not yet influenced the dynamics of the shock.

Unified Astronomy Thesaurus concepts: Shocks (2086); Filamentary nebulae (535); Supernova remnants (1667)

1. Introduction

The Cygnus Loop supernova remnant (SNR) is classified as “middle-aged,” and is about 20,000 yr old (Fesen et al. 2018). The overall morphology of the remnant is shell-like at all wavelengths from gamma-rays to the radio. Around the perimeter of the remnant, there are a number of recent shocks with ages of one to a few thousand years where the blast wave encounters dense clouds. While the bulk of the optical/UV emission arises from radiative shocks in regions where the shock fronts interact with these relatively dense clouds, fainter nonradiative shocks are detected around about half the remnant’s perimeter (Levenson et al. 1998). These faint nonradiative shocks arise from the primary shock front as it encounters lower-density and at least partially neutral interstellar material. In these filaments, the emission arises from neutral atoms that are excited prior to being ionized (Chevalier et al. 1980), thus manifesting themselves as thin filaments of pure H α λ 6563 (and sometimes other Balmer-line) emission. There are a few isolated regions along these Balmer filaments that are just cooling and hence starting to become radiative. These transition shock fronts have been identified in deep [O III] λ 5007 images, where the emission “turns on” at locations along an otherwise nonradiative filament (Hester et al. 1994).

Two of the prominent transition shocks, well separated from other strong emission, were imaged in H α and [O III] by Blair et al. (2005) using the Wide Field Planetary Camera-2 (WFPC2) on the Hubble Space Telescope (HST). One of these

filaments (their Field #1) had been imaged four years previously in H α with the same instrument (Blair et al. 1999). Based on the two epochs of HST imaging, Blair et al. (2005) measured a proper motion of $0''.070 \pm 0''.008$ yr⁻¹ for this filament. Ultraviolet spectra of the filament have been obtained using the International Ultraviolet Explorer (IUE; Raymond et al. 1983), the Hopkins Ultraviolet Telescope (HUT; Long et al. 1992), the Space Telescope Imaging Spectrograph (STIS) on the HST (Sankrit et al. 2000) and the Far-Ultraviolet Spectroscopic Explorer (FUSE; Sankrit & Blair 2002). The strengths of high-ionization lines measured in these spectra are best reproduced by a ~ 180 km s⁻¹ shock with a preshock density in the range 2–4 cm⁻³. Katsuda et al. (2016) have presented high-resolution optical spectra from Subaru along a crosscut at one location on the filament. They identify four individual shock fronts within the $\sim 10''$ width of the filament, each sharp feature being a tangency between the line of sight and the surface of the rippled shock (Hester 1987). They find that the width of the broad component of the H α emission decreases from the outermost to the innermost shock, which they suggest is due to different shock speeds.

Blair et al. (2005) combined the proper motion of the filament and an estimate of the shock speed (based on the UV studies) to derive a distance to the Cygnus Loop of 540 pc, with an upper limit of about 640 pc. Medina et al. (2014) measured the broad-component width of H α at several locations to derive shock speeds, and using proper motion measurements from Salvesen et al. (2009), they estimated a much larger distance of 890 pc to the remnant. Raymond et al. (2015) found efficient thermal equilibration in the postshock gas using measurements of the He II λ 1640 line and the C IV λ 1550 doublet in HST Cosmic Origins Spectrograph (COS) spectra, and revised the Medina et al. (2014) estimate downward to 800 pc. A different

Table 1
HST Imaging Observations

Obs. Date	Obs. Time ^a	Prop. ID	Instrument	Filter	t_{exp} (s)
1997 Nov 16	1997.874	07289	WFPC2	F656N	7400
2001 Oct 19	2001.797	09080	...	F502N	5200
2001 Nov 14	2001.869	F656N	7400
2020 Jul 01	2020.498	15893	WFC3	F656N	7414
2020 Jul 01	2020.499	F502N	7414

Note.

^a Decimal years, UT, at the start of the observation.

method, based on Gaia parallaxes toward stars in the direction of the Cygnus Loop, was used by Fesen et al. (2018) to calculate a precise value for the distance. Based on the Gaia DR3 release, their initial result was recently updated to a distance of 725 ± 15 pc to the center of the remnant (Fesen et al. 2021), which is the value we will assume in this paper.

Here, we present new HST Wide Field Camera-3 (WFC3) $H\alpha$ and [O III] images of the Field #1 filament (which we henceforth refer to as “Filament 1”). We use the new and previous epoch $H\alpha$ data to measure proper motions along the leading edge of the shock front. With a second epoch of [O III], we measure the proper motions of the [O III] emitting portions of the filament for the first time, and also discuss the properties of a radiative knot that is part of Filament 1 in the images.

2. Observations

The Cygnus Loop was observed on 2020 July 1, using HST/WFC3, through the UVIS channel narrowband filters, F656N and F502N, which transmit $H\alpha$ and [O III] $\lambda 5007$ emission, respectively. No continuum band was necessary, because the star density on the sky is low and the filaments are extended. The position angle was chosen to include the nonradiative filament of interest on a single UVIS CCD and fainter filaments toward the interior of the remnant on the other CCD. For each observation, a primary two-point dither was used to cover the interchip gap, along with a secondary three-point dither pattern to recover fine structure. Preflash exposures were used to mitigate the effects of charge transfer inefficiency. The total exposure time on target through each filter was 7414 s.

The previous HST/WFPC2 observations of Filament 1 were obtained in 1997 (Blair et al. 1999) and 2001 (Blair et al. 2005). In the first epoch, only an $H\alpha$ image was obtained, while in the second, both $H\alpha$ and [O III] images were obtained. Some details about the observations used in this study are given in Table 1. We use the calibrated images obtained from the MAST archive for our analysis. In the case of Epoch 1 and 2 data, these are the versions available in the Hubble Legacy Archive⁴ (HLA), and for which we have updated the astrometry to Gaia coordinates, as recommended.

The Epoch 3 WFC3 $H\alpha$ and [O III] images are shown in Figure 1. The brighter filament seen closer to the top of the FOV is Filament 1, which is the focus of this paper. Faint [O III] emission may be traced along the filament, but it is only toward the right edge that it becomes prominent. Two-color images of the [O III] emitting locations along the filament are shown in Figure 2.

3. Results

3.1. Proper Motion Measurements

We used the Epoch 2 and 3 $H\alpha$ images to determine an improved proper motion measurement for the leading edge of Filament 1. Profiles across the filament were obtained using the “projection” regions in the SAOImageDS9 software package. The regions were defined using the Epoch 2 image. The orientations and widths of the projections were determined by eye, overlaying the short-axis lines on a highly zoomed-in display. For each projection, the counts pixel^{-1} along the length, and averaged over the width were obtained for both Epoch 2 and Epoch 3 images, and the peak-flux positions corresponding to the leading filament were determined from these profiles. The peaks were determined by inspecting the images and were defined either to be the pixel location with the highest flux, or in some cases midway between two pixel locations of about equal flux. The proper motions were calculated as the separation between the peaks in Epoch 2 and Epoch 3 divided by the time interval, 18.63 yr, between the observations (Table 1).

The peak-flux positions are accurate to about half a pixel, which corresponds to $0''.05$ for the WFPC2 image and $0''.02$ for the WFC3 image. The astrometry for both epochs were based on Gaia positions. However, residual differences between WFPC2 and WFC3 images are typically present, because for the former, the WCS is transformed as a last step to align the already calibrated images with Gaia coordinates. In order to check the accuracy of the relative astrometry between these images, we identified 20 stars of moderate brightness, 10 on each side of the filament, and found that their WCS coordinates differed on average by about $0''.12$. The error in the peak-flux separation is therefore about $0''.13$, which translates to an error in the proper motion of 7 mas yr^{-1} .

The projection regions are shown overlaid on the Epoch 2 $H\alpha$ image in the top panel of Figure 3. The labels are the region designations, and the numbers are the measured proper motions. The bottom panel directly shows the motion of the shock front between the two epochs. The proper motions range from 55 to 85 mas yr^{-1} , with a typical value of 70 mas yr^{-1} . We also measured the proper motions at these locations between Epoch 1 and 2 and found that they were the same as between Epochs 2 and 3, well within the errors and with no systematic offset. Thus, the filament is neither accelerating nor decelerating at a measurable level. The typical proper motion we find is consistent with the average value of $70 \pm 8 \text{ mas yr}^{-1}$ determined for Filament 1 as a whole by Blair et al. (2005) based on Epoch 1 and 2 images. (We note that their reported error does not refer to an individual proper motion measurement, but rather is the standard error of a set of several such measurements.)

The proper motions vary smoothly along sections of the filament, and they are consistent with a “rippled sheet” morphology viewed edge-on (Hester 1987). The morphology in Figure 3 shows that, at many places along the filament, the ripples are at angles of order 10° to the average shock normal. The most abrupt change in proper motion is between p06 and p07, which suggests they are distinct parts of the shock front, separated in space in the line-of-sight direction. The image shows that the leading edges at these two locations are clearly different ripples, based on their continuity across an “X” crossing.

⁴ <https://hla.stsci.edu>

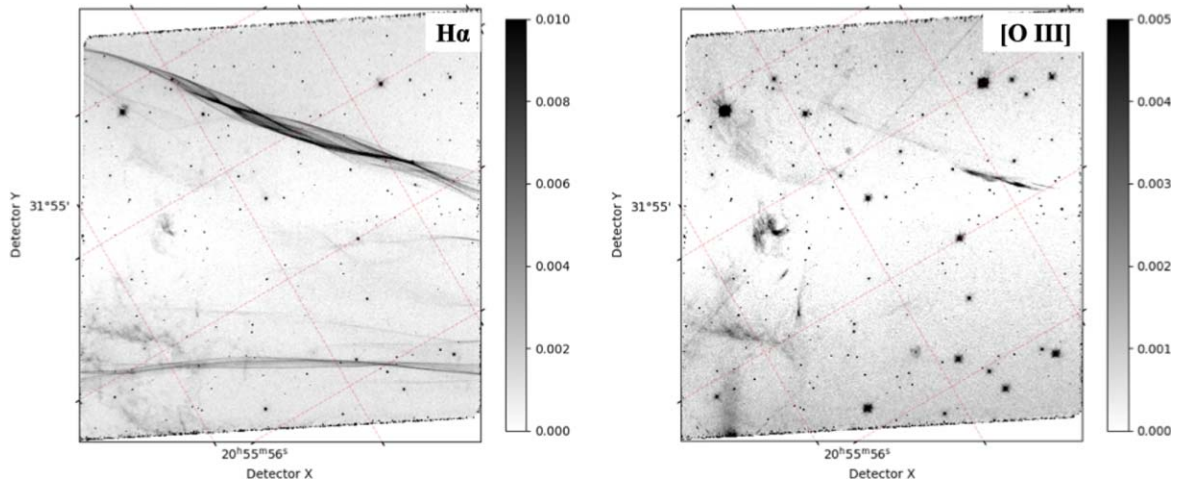


Figure 1. Processed and combined HST/WFC3 full-field images of a region in the NE Cygnus Loop. Left panel: F656N ($H\alpha$). Right panel: F502N ([O III]) emission. The display is linear and has been scaled to show the faint filaments. The units on the colorbars are counts s^{-1} . The field of view is about $160'' \times 160''$. North (top right corner) and east (top left corner) are defined by the grid lines.

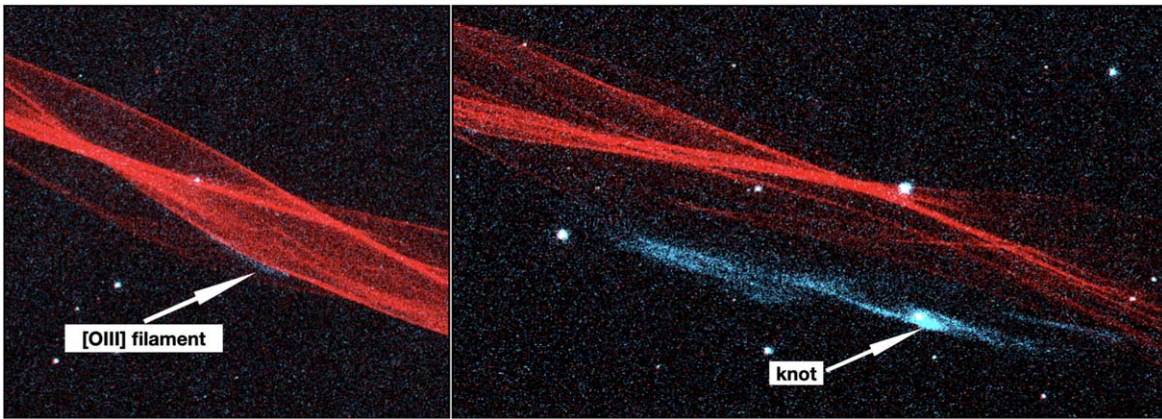


Figure 2. Epoch 3 images of two regions along Filament 1, with F656N ($H\alpha$) in red and F502N ([O III]) in cyan. Left panel: very faint [O III] emission at the location near the upper left end of the filament as seen in Figure 1. Right panel: the brighter [O III] region at the bottom right end of the filament.

The $H\alpha$ profiles along projection regions p05–p08 are shown in Figure 4. For each profile, approximate backgrounds have been subtracted and the Epoch 2 peak has been set as the zero point of the distance scale. These profiles are representative of our sample and give an idea of how well we are able to measure the proper motions. The specific locations shown will be discussed further in Section 4.

The count rates in the profiles are sampled at the pixel scale, which is $0''.1$ for WFPC2 and $0''.04$ for WFC3. These can be converted to physical units using the formula for emission line sources given in Section 9.4.3 of the WFC3 Instrument Handbook (Version 14.0, 2022 January). The system throughput (QT_s) values for the F656N filters are 0.11 for WFPC2 and 0.22 for WFC3, which yield conversion factors for count rates to flux of 5.97×10^{-16} and 3.04×10^{-16} , respectively. As an example, we have obtained the surface brightnesses of regions $3''.7$ long and $0''.6$ wide that encompass the leading shock front at position p08. The total count rates are 4.4 ± 2.1 cts s^{-1} in the WFPC2 image, and 9.7 ± 3.1 cts s^{-1} in the WFC3 image. These correspond to surface brightnesses of $2.6 \pm 1.2 \times 10^{-15}$ and $2.9 \pm 0.9 \times 10^{-15}$ erg s^{-1} cm^{-2} $arcsec^{-2}$ at Epochs 2 and 3, respectively. The relative count rates at other locations along the shock front are approximately the same as for the p08 section we have considered, and thus, within our measurement errors, the

$H\alpha$ intensity of the shock has remained about the same between the two epochs. The regions used for the flux measurement contain about 220 pixels in the WFPC2 image and 1400 pixels in the WFC3 image. The emission is intrinsically faint and the structures are sharp, and the errors are large because they are dominated by the detector dark rate (~ 0.008 e $^{-1}$ s $^{-1}$ pixel $^{-1}$ for WFPC2 and ~ 0.003 e $^{-1}$ s $^{-1}$ pixel $^{-1}$ for WFC3).

The bright [O III] emission is less sharply defined than the $H\alpha$, but the time interval between the epochs is sufficient for obtaining proper motions using the same method. Three projection regions were defined, and the peak-flux separations measured. The time interval between observations is 18.70 yr, and the proper motions are 45 mas yr^{-1} for all the locations. Figure 5 is a two-color image showing the motion of the filament. The projection regions are overlaid, along with their labels, and the measured proper motions. The profiles along these regions are shown in Figure 6. As in Figure 4, approximate backgrounds have been subtracted, and the distance zero point is at the peak of the Epoch 2 emission profile.

The proper motion of the [O III] emitting locations is significantly lower than those of the $H\alpha$ filaments (Figure 3), which implies that the shock speeds are lower. The lower shock speed implies a shorter cooling time, which is consistent with

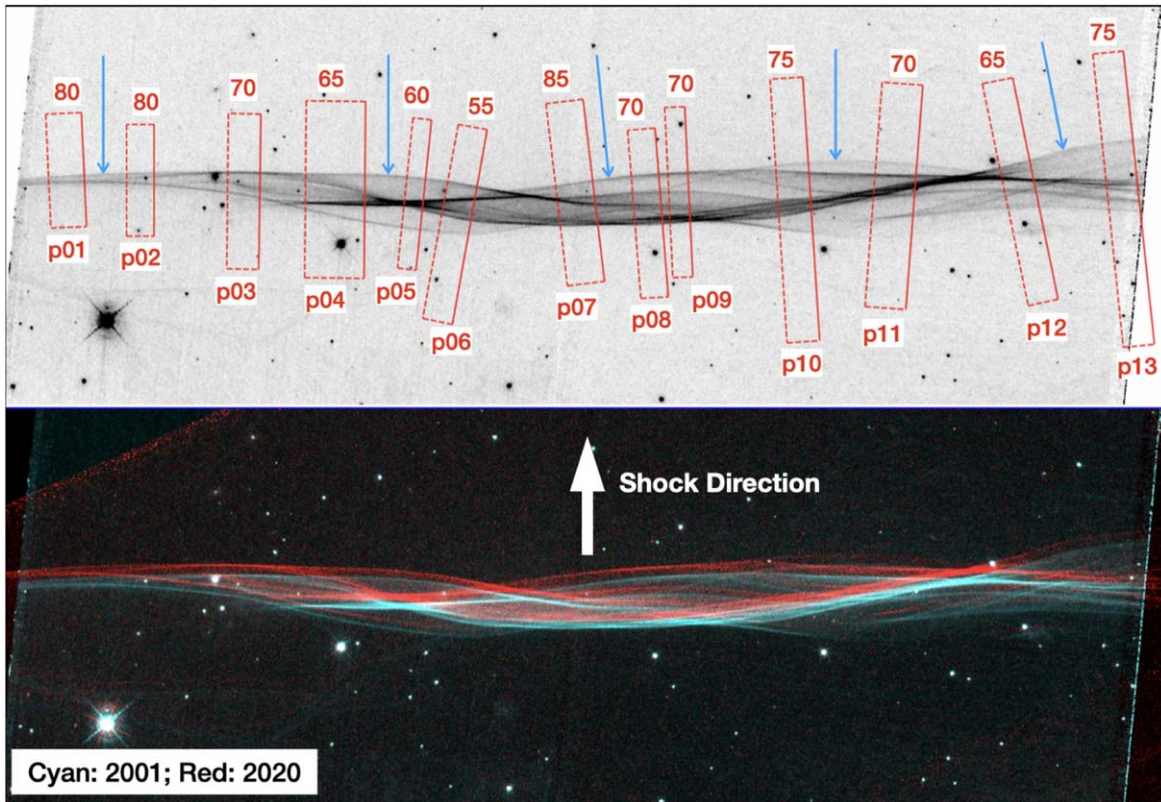


Figure 3. Top panel: Epoch 2 $H\alpha$ image of Filament 1. The labeled red boxes are ds9 projection regions. The numbers at the top of each box are the measured proper motions in mas yr^{-1} of the leading shock front at each location. The leading edge is indicated by blue arrows at several locations along the filament. Bottom panel: Epoch 3 (red) and 2 (cyan) $H\alpha$ images of the same field. The motion of the shock fronts against the background of stars (white) is clearly seen, and it is evident that they have retained their overall structure with no discernible changes. The excellent alignment of the stars in the images is noteworthy.

the strong [O III] emission from the recombined gas in the postshock region. By this stage, the preshock gas has been ionized and the Balmer filaments have disappeared at these locations.

3.2. Radiative Knot

One of the features located along Filament 1 is a knot of emission that is prominent in the [O III] image (Figure 2) and is moving along with the rest of the filament (Figure 5). A close-up of the knot and the nearby filament at Epochs 2 and 3 is shown in Figure 7. Also shown overlaid are the ds9 regions that we use for analysis. In Epoch 3, the knot overlaps a star and they cannot be easily separated. Therefore, we restrict our attention to an elliptical region including the brightest portion of the knot. The box region is on the q02 filament (Figure 5).

The [O III] surface brightnesses of the knot and filament at each epoch were obtained by taking the total count rates and areas for the regions and converting them to physical units using the formula mentioned above in Section 3.1. For the F502N filters, the QT_λ values are 0.058 for WFPC2 and 0.23 for WFC3, which yield count rate to flux conversion factors of 1.51×10^{-15} and 3.81×10^{-16} , respectively.

The elliptical regions are $0''.4 \times 0''.25$ with an area of 0.31 arcsec^2 . In the Epoch 2 image, the region comprises 32 pixels and the total count rate is 0.97 cts s^{-1} . The Epoch 3 region has 200 pixels and a total count rate of 4.24 cts s^{-1} . The error is dominated by the background noise in each pixel. We sampled several background regions and found a standard error of $0.002 \text{ cts s}^{-1} \text{ pixel}^{-1}$ for both the WFPC2 and WFC3

Table 2
Shock-driving Pressures

Region	$n_0(\text{cm}^{-3})$	$v_s(\text{km s}^{-1})$	$n_0 v_s^2$ ($10^{14} \text{ cm}^{-1} \text{ s}^{-2}$)	References
Blast wave	0.4	348	4.8	[1] based on [2–4]
Filament 1	2.0	200	8.0	[5], [6]
XA region	5.0	150	11.3	[7]
XA edge	1.6 ^a	180	5.1	[8], [9]
Spur	6.0	120	8.6	[10]
SE cloud ^b	5.8	[11]
SW breakout cloud ^b	5.4	[12]
Western cloud	8.2	130	13.8	[13]

Notes.

^a Assuming a path length of $5 \times 10^{18} \text{ cm}$ through the [Ne V] emitting region.
^b In cases where pressures have been reported in units of $[\text{dyne cm}^{-2}]$, we convert to $[\text{cm}^{-1} \text{ s}^{-2}]$ using a mean atomic mass of $1.34 m_H$, which assumes that $[\text{He}] = 10.93$ on a log abundance scale where $[\text{H}] = 12.0$ (Raymond et al. 1988).

References. (1) Fesen et al. 2018; (2) Salvesen et al. 2009; (3) Medina et al. 2014; (4) Raymond et al. 2015; (5) Raymond et al. 1983; (6) Hester et al. 1994; (7) Sankrit et al. 2014; (8) Szentgyorgyi et al. 2000; (9) Sankrit et al. 2007; (10) Raymond et al. 1988; (11) Graham et al. 1995; (12) Patnaude et al. 2002; (13) Raymond et al. 2020b.

images. Thus, for the knot, the error on the count rate is 6.6% for Epoch 2 and 9.4% for Epoch 3. The box regions are $2''.5 \times 0''.4$, and they contain 99 pixels in the WFPC2 image and 637 pixels in the WFC3 image. The total count rates for the

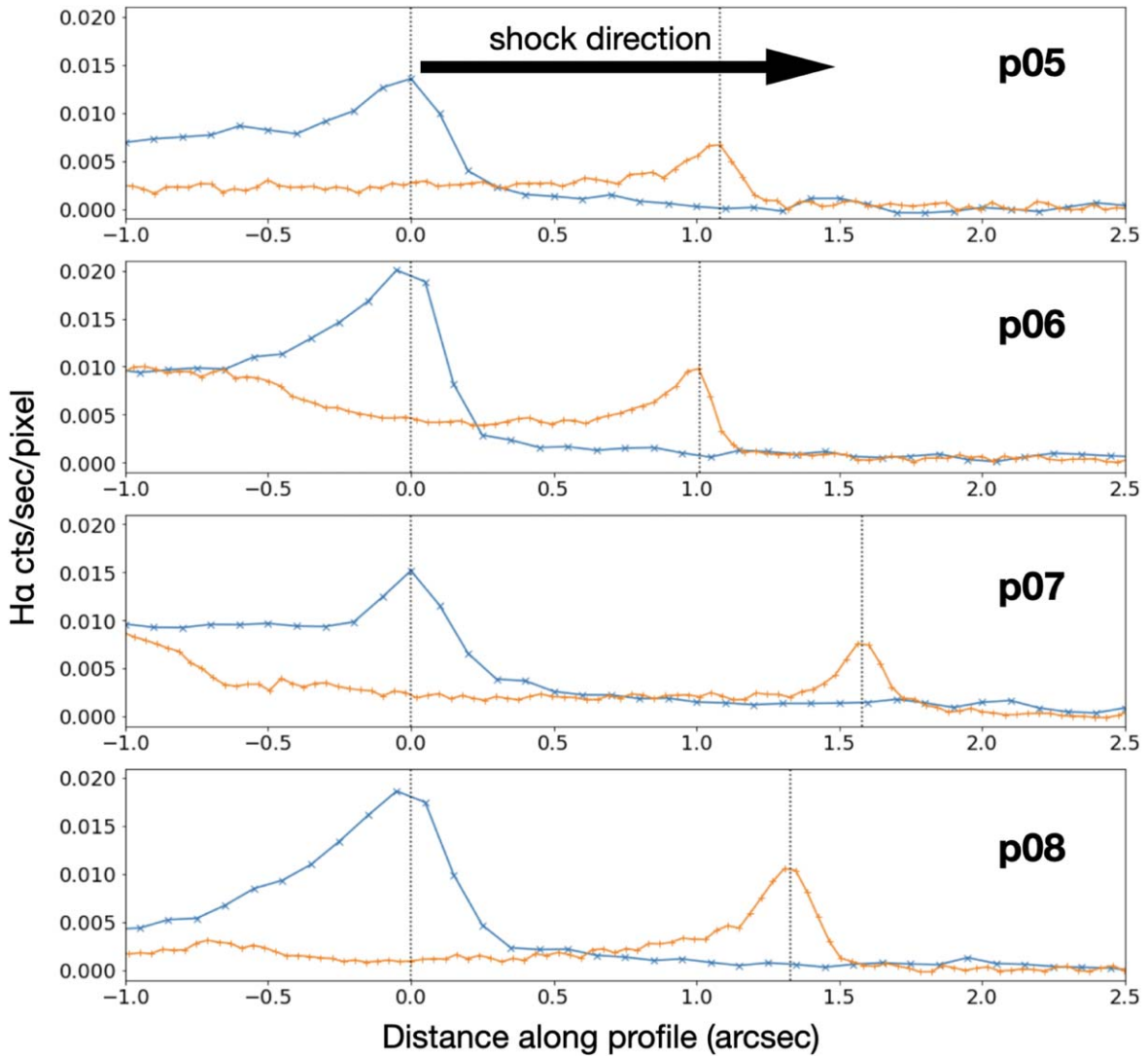


Figure 4. $H\alpha$ emission along a selection of profiles shown in Figure 3. Epoch 2 profiles are shown in cyan with “x” symbols and Epoch 3 in orange with “+” symbols. The count rates are per-pixel averaged across the width of the projection. It should be noted that the conversion of count rates to fluxes differs for Epochs 2 and 3, because the WFC2 and WFC3 pixel sizes are different as are the filter sensitivities (see text for details).

two epochs are 0.98 cts s^{-1} and 3.50 cts s^{-1} , with errors of 20% and 36%, respectively.

Using the conversion factors (and with the percentage errors propagating unchanged), we get the following surface brightness measurements in units of $10^{-15} \text{ erg s}^{-1} \text{ cm}^{-2} \text{ arcsec}^{-2}$: at Epoch 2, 4.56 ± 0.30 for the knot and 1.49 ± 0.30 for the filament; at Epoch 3, 5.14 ± 0.48 for the knot and 1.33 ± 0.48 for the filament. Taken at face value, these measurements suggest that the knot has become brighter by about 12% between the two epochs. (The error bars overlap, so this result should not be overinterpreted.) The nearby filament is 3–4 times fainter than the knot, and its brightness has remained unchanged within errors between the two epochs.

A brightening of the [O III] knot would be expected as the gas recombines from O^{3+} to O^{2+} , but the uncertainty may be dominated by how precisely the extraction apertures capture the same section of the shock for the two epochs. If the preshock density ahead of the knot is about 2 times that ahead of the filament, it would explain its higher brightness. This would also explain the increase in brightness between Epochs 2

and 3, because the higher density will result in a shorter cooling and recombination time.

4. Physical Properties of the Shock

At the leading edges of the nonradiative filaments, the proper motion measured by the peak $H\alpha$ emission scales linearly with the shock velocity, because projection effects are minimized. For a distance of 725 pc to the remnant (Fesen et al. 2021), the shock velocity $v_s(\text{km s}^{-1}) = 3.44 \times \Delta\theta/\Delta t$ (mas yr^{-1}). The measured proper motions (Figure 3) imply that the shock velocities lie in the range 190–290 km s^{-1} , with a median value of about 240 km s^{-1} .

If we assume isobaric conditions, then the ram pressure driving the shock front is constant at all locations. This pressure is proportional to $n_0 \times v_s^2$, where n_0 is the preshock number density and v_s is the shock velocity. Ultraviolet spectra of Filament 1 have been modeled to determine the shock velocities and preshock densities (Raymond et al. 1983; Long et al. 1992; Sankrit et al. 2000; Sankrit & Blair 2002). Although there are many sources of uncertainty, in particular in

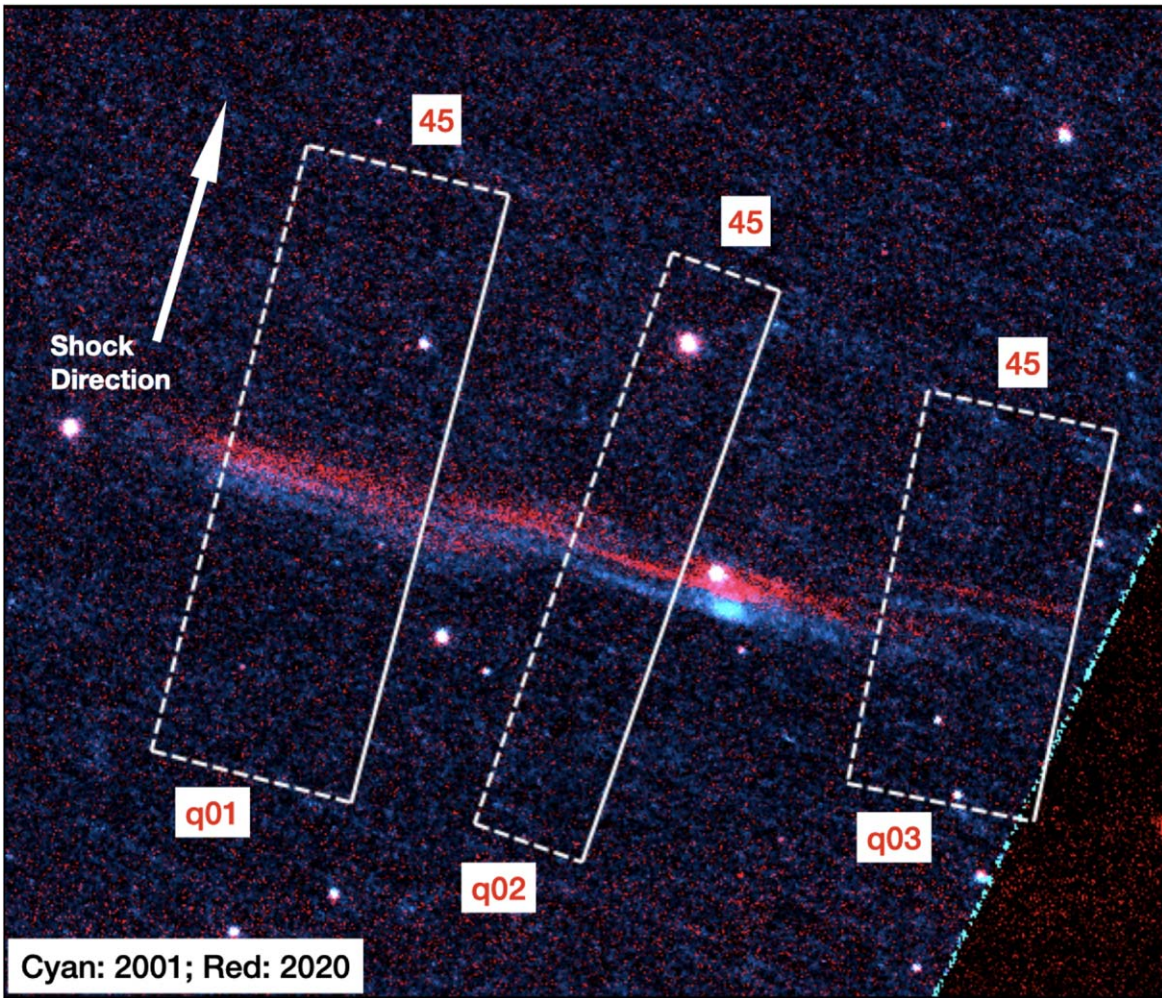


Figure 5. Two-color image showing the brightest [O III] portion of Filament 1, with Epoch 2 in cyan and Epoch 3 in red. As in Figure 3, the labeled boxes are ds9 projection regions, and the numbers the proper motions in mas yr^{-1} .

the estimate of the preshock density, which depends on assumptions about the filament geometry, all the data suggest that shock velocities of about 180 km s^{-1} are running into material with a density in the range $2\text{--}4 \text{ cm}^{-3}$. In our analysis, we use the ram pressure quoted by Raymond et al. (1983) of $8 \times 10^{14} \text{ cm}^{-1} \text{ s}^{-2}$. For the shock velocities observed, the preshock densities lie in the range 0.95 to 2.2 cm^{-3} , with a median value of 1.4 cm^{-3} .

The variation in the preshock density to some extent determines the shape of the Balmer filament. Along the shock front between p01 and p06, separated by $\sim 1'$, the preshock density changes by a factor of two, from 1.1 cm^{-3} to 2.2 cm^{-3} , with about 16% of the rise happening in the $6''$ between p05 and p06. The change is even sharper between p07 and p08, where over a $10''$ section of the filament, the preshock density changes by 55%, from 0.9 to 1.4 cm^{-3} .

The velocity gradient between closely spaced locations can be used to estimate the vorticity in the plane of the shock front, $\omega = \Delta v_s / \Delta s$, where Δs is the length along the front. Since both quantities scale linearly with distance, we can use angular units, which yields $\omega_{\text{p05-p06}} = 5/6000 \text{ yr}^{-1}$ and $\omega_{\text{p07-p08}} = 15/10,000 \text{ yr}^{-1}$. The vorticity is the inverse of the eddy turnover time, which is the timescale on which turbulence may be expected to develop (Raymond et al. 2020a). However, it should also be noted that Spangler (2022) finds there are cases where

irrotational fluid flows (zero vorticity) may still yield observed velocity gradients using the method described above. Our vorticity estimates thus correspond to turnover times of ~ 1200 and $\sim 670 \text{ yr}$ for the portions of the filaments considered. These numbers are approximations, because we need the velocity gradients in all directions in order to determine the true vorticity. However, the average value of $\sim 950 \text{ yr}$ may be taken as a reasonable estimate for the turnover time. The optical morphologies show no obvious sign of turbulence. This implies that the effective shock age, defined as the time since the supernova blast wave encountered the density enhancement at this location, is less than about 1000 yr .

An independent estimate of the shock age for Filament 1 may be obtained using the properties of the [O III]-emitting portion of the filament. We assume that the proper motion is directly proportional to the shock velocity, and that the ram pressure driving the shock is the same as that for the $\text{H}\alpha$ filament. The measured proper motion, 45 mas yr^{-1} , implies a shock velocity of 155 km s^{-1} and subsequently a preshock density of 3.4 cm^{-3} . Then, the strength of the [O III] emission and the lack of detectable $\text{H}\alpha$ emission imply that the age of the shock, t_{shock} , is about equal to the cooling time of the shocked gas. For the shock velocity and preshock density quoted above, the shock age is $\approx 800 \text{ yr}$ (Hartigan et al. 1987), which is

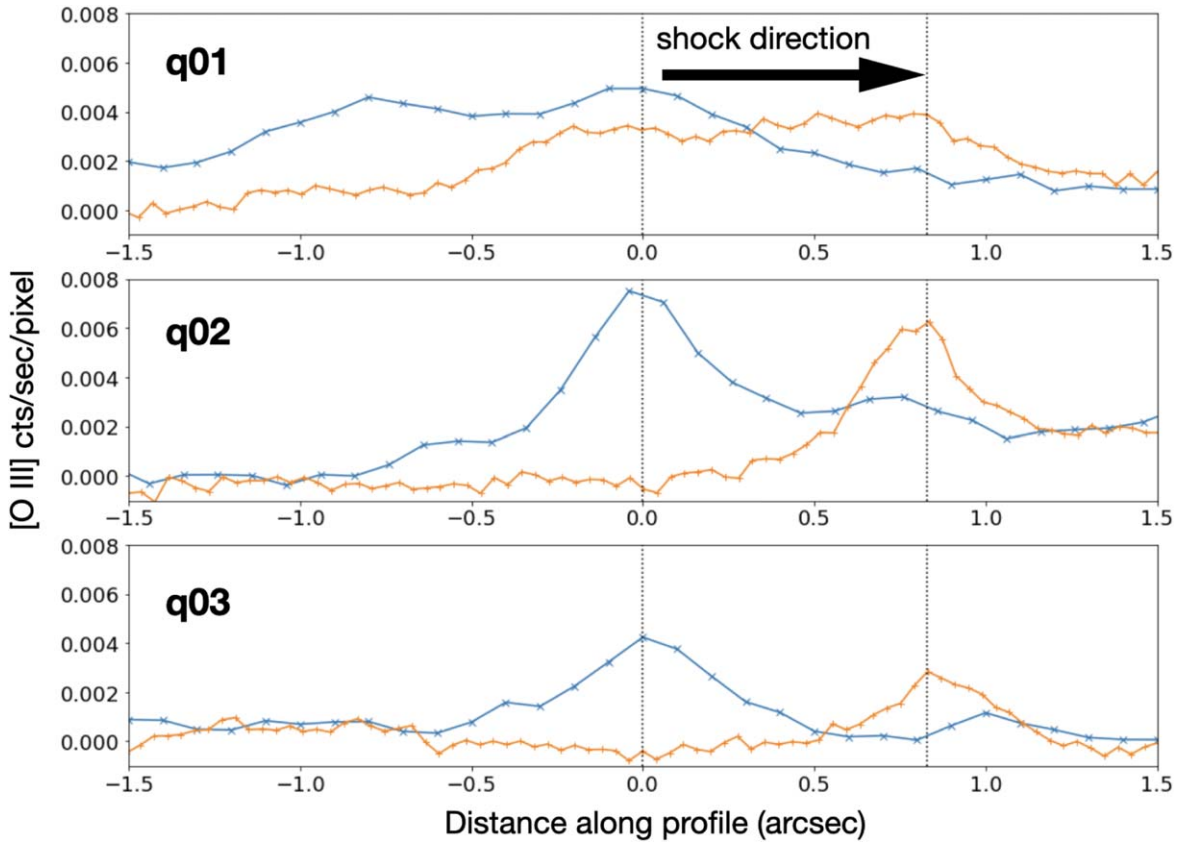


Figure 6. [O III] emission along the profiles shown in Figure 5. Epoch 2 profiles are shown in cyan with “x” symbols and Epoch 3 in orange with “+” symbols.

consistent with turbulence not yet having influenced the dynamics of the shocked gas.

5. Discussion

The nonradiative shocks around the Cygnus Loop are among the slowest such shocks that have been observed in SNRs (e.g., Ghavamian et al. 2001). The measured velocities range from about 190 km s^{-1} (in Filament 1) to about $350\text{--}400 \text{ km s}^{-1}$ further along the perimeter toward the NE (Salvesen et al. 2009; Medina et al. 2014). The shock velocity at one of these locations (Raymond et al. 2015), normalized to the new distance, is at the lower end of this range, and it is taken to be representative of the supernova blast wave by Fesen et al. (2018). The preshock density is 0.4 cm^{-3} (see their Table 3), and so the shock-driving pressure is $4.8 \times 10^{14} \text{ cm}^{-1} \text{ s}^{-2}$. The shock-driving pressure at Filament 1 is about 70% higher. Before discussing the implications of this difference, we consider the overall variation in shock-driving pressures at other locations in the Cygnus Loop.

In Table 2, we list the values of $n_0 \times v_s^2$ measured at several locations in the Cygnus Loop, starting with the filament tracing the blast wave and moving counterclockwise around the remnant. The XA region is part of the bright radiative shock–cloud interaction on the eastern limb of the remnant (Hester & Cox 1986). The XA edge is the remnant boundary east of the radiative shock, which is demarcated by a transition shock emitting $[\text{Ne V}]\lambda 3425$ (Szentgyorgyi et al. 2000). The Spur is a clearly defined $1/5$ long feature that lies in the same cloud a few arcminutes NW of the XA region (Hester et al. 1983; Raymond et al. 1988). The SE cloud is an isolated shocked

cloud about $45'$ along the perimeter going counterclockwise from XA (Fesen et al. 1992). The SW breakout cloud is on the western limb of the southern “breakout” region of the Cygnus Loop, and it consists of a mix of nonradiative, transitioning, and radiative filaments (Patnaude et al. 2002). The western cloud is a bright, radiatively shocked cloud on the western edge of the remnant, and it was recently studied in detail by Raymond et al. (2020a, 2020b).

The pressure following shock–cloud interactions is time dependent (McKee et al. 1987; Klein et al. 1994). The driving pressure increases by up to a factor of six for a planar shock, and up to a factor of three for bow shocks around smaller clouds. Following the rise to maximum, the pressure falls back to the pressure of the shocked intercloud medium. Although there are fairly large uncertainties associated with each of the values for shock-driving pressure listed in Table 2, an overall trend can be discerned. The XA edge and SW breakout cloud are both associated with recent shocks that have not become fully radiative, and consequently the pressure is only slightly higher than that driving the blast wave. The highest pressures are associated with the bright radiative shocks in the XA region and in the western cloud, about 2–3 times that for the blast wave. These are most probably due to the shock having decelerated rapidly as it recently encountered a denser cloud, and the pressures are close to the maximum levels they can reach. The remaining regions, the Spur and the SE cloud, are places where the shock–cloud interactions are more mature. Therefore, although the preshock densities are similar to those in the XA region and western cloud, the driving pressures have fallen from their peak values.

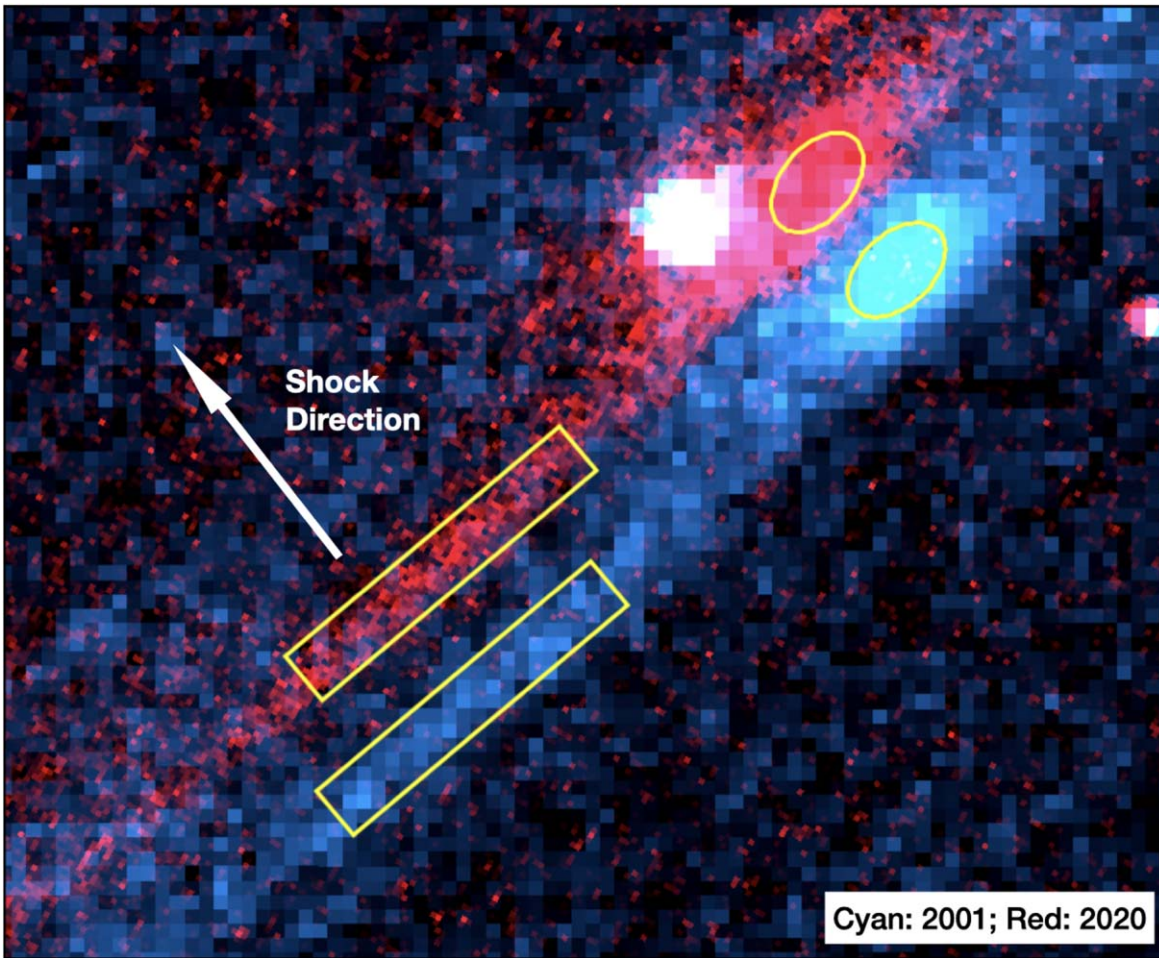


Figure 7. Two-color image zooming in on the [O III] knot, with Epoch 2 in cyan and Epoch 3 in red. The yellow ellipses are ds9 regions $0''.4$ major axis and $0''.25$ minor axis, including the brightest portion of the knot, and the boxes are $2''.5 \times 0''.4$ regions along a nearby filament. The larger pixels in the WFPC2 image (Epoch 2) are evident.

The high driving pressure and the low shock velocity responsible for Filament 1 indicate that a reflected shock has developed recently, which in turn is most easily explained if the shock wave has hit a density jump. Based on their detailed study of the region, Hester et al. (1994) concluded that the pressure could be explained by a blast wave hitting the walls of a cavity with a density about 10 times that of the interior. In contrast, the relatively modest difference in pressures, between the XA edge and SW breakout cloud on the one hand and the blast wave on the other, does not require such a sudden jump.

A long-standing question about the Cygnus Loop is whether it is better described as an explosion in a cavity where the supernova shock has recently reached the cavity walls, or as a Sedov–Taylor blast wave interacting with dense clouds over some fraction of its surface. The cavity picture for the remnant was first suggested by Charles et al. (1985). They note that the X-ray temperature decreases with distance from the center and the emission measure increases, as predicted by the Sedov–Taylor model. However, they attributed the optical emission to dense clouds overrun by the blast wave, and went on to argue that a uniform distribution of clouds would give rise to X-ray emission from the interior that would give a center-filled morphology rather than the limb-brightened appearance that is observed. They therefore concluded that the SN explosion occurred in a cavity produced by the precursor star. Further

evidence for the cavity remnant picture was provided by the analysis of high angular resolution X-ray data using ROSAT HRI that showed significant limb brightening on small scales (Levenson et al. 1997), deep $H\alpha$ images showing a near-complete circular shell containing nonradiative filaments (Levenson et al. 1998) and ROSAT PSPC data that showed a thin shell of enhanced soft X-ray emission around almost the entire remnant (Levenson et al. 1999). Fang et al. (2017) present the most complete model for the Cygnus Loop as an explosion in a cavity, with the precursor star moving toward the north and a polar wind pointed toward the northeast, with a slow phase followed by a faster phase. They predict an overall shape very much like that observed, though it is not clear whether they predict the large variations in preshock density indicated in Table 2.

In one version of the cavity explosion scenario, all the dense clouds were pushed to the edge of the cavity via the rocket effect, which accounts for the near-circular morphology of the optical and X-ray emission (e.g. Charles et al. 1985). When examined in detail, however, the optical morphology of the Cygnus Loop is dominated by departures from symmetry. Most recently, Fesen et al. (2018) have used composite multi-wavelength images to provide a fairly complete picture of the shock interactions around the remnant. The shock wave is currently encountering a very large dense cloud to the west, a

smaller, less dense cloud to the east, and one or two clouds that account for the two north–south filament complexes that run in projection across the center and west–center parts of the remnant, along with three parsec-scale clouds in the SE (Fesen et al. 1992), the SW (Patnaude et al. 2002), and the NE (Katsuda et al. 2016). The SW cloud is in the southern blowout region, so a reasonable estimate is that there are two parsec-scale clouds in the outer 1–2 pc shell of the SNR, or one cloud per 400 pc^3 . The volume of the Cygnus Loop is about $23,000 \text{ pc}^3$, so if the small clouds were randomly distributed, about 500 would have been engulfed. Assuming a density of 1 cm^{-3} , each cloud would have a mass around $0.1 M_{\odot}$, for a total mass of $50 M_{\odot}$. That is a significant—but not dominant—fraction of the roughly $100 M_{\odot}$ swept up by the blastwave.

An explosion in an undisturbed interstellar medium (ISM) between the clouds could produce a Sedov–Taylor SNR. Fesen et al. (2018) have shown that the shock speed, radius, and preshock density of the northern Cygnus Loop filament (Raymond et al. 2015) are consistent with a Sedov–Taylor solution with a typical SN energy. Unfortunately, the picture of a Sedov–Taylor blast wave in a medium with randomly placed clouds does not predict a morphology beyond the expectation that the SNR will be flattened where it encounters dense clouds like those in the northeast and west.

The Filament 1 properties presented here are not, by themselves, sufficient to distinguish between the two possibilities of the preshock medium being a cavity wall or an interstellar cloud. If the properties of a much larger sample of nonradiative shocks around the Cygnus Loop could be investigated, it would be possible to determine whether they are compatible with a Sedov–Taylor shock or if they require a recent encounter with a density enhancement. If a sufficiently large fraction of the Balmer-dominated filament shell exhibits slower shock velocities and higher shock-driving pressures, the cavity-wall scenario would be the simpler and more likely interpretation.

6. Summary

In this paper, we have used multi-epoch HST $H\alpha$ and [O III] images to study the evolution of a Balmer-dominated filament in the northeast region of the Cygnus Loop SNR. The long time baseline, the high angular resolution of HST, and the independently established distance to the Cygnus Loop have allowed us to determine the shock velocities, which are among the lowest measured for nonradiative shocks in SNRs. The shock front has been moving smoothly into the surrounding medium over a ~ 20 yr period, with no measurable deceleration and no drastic changes in filament morphology or brightness. Ahead of the main $H\alpha$ filament, the preshock densities vary by a factor of a little over two. An [O III] knot toward one end of the filament has increased in brightness, suggesting that the shock is running into a region of somewhat higher density at that location. The shock age is less than the eddy turnover timescale, which implies that turbulence has not yet influenced the dynamics of the shock. The shock-driving pressure is a almost a factor of two higher than that driving the main blast wave, indicating that the shock recently hit a density

discontinuity. This may have been an interstellar cloud, or the cavity wall in the case where the Cygnus Loop was a cavity remnant.

R.S. was supported in part by grant HST-GO-15893.001-A to the Space Telescope Science Institute. W.P.B. acknowledges grant HST-GO-15893-002-A to the Johns Hopkins University and the Center for Astrophysical Sciences at JHU for partial support during the period of this work. We thank the referee for several useful suggestions, which improved the content and clarity of the paper.

The data used in this study and presented in this paper were obtained from the Mikulski Archive for Space Telescopes (MAST) at the Space Telescope Science Institute. Observations may be accessed via [10.17909/q7ag-v025](https://doi.org/10.17909/q7ag-v025).

Facilities: HST(WFPC2, WFC3).

Software: SAOImage DS9 (Joye & Mandel 2003).

ORCID iDs

Ravi Sankrit  <https://orcid.org/0000-0001-8858-1943>

William P. Blair  <https://orcid.org/0000-0003-2379-6518>

John C. Raymond  <https://orcid.org/0000-0002-7868-1622>

References

- Blair, W. P., Sankrit, R., Raymond, J. C., et al. 1999, *AJ*, 118, 942
 Blair, W. P., Sankrit, R., & Raymond, J. C. 2005, *AJ*, 129, 2268
 Charles, P. A., Kahn, S. M., & McKee, C. F. 1985, *ApJ*, 295, 456
 Chevalier, R. A., Kirshner, R. P., & Raymond, J. C. 1980, *ApJ*, 235, 186
 Fang, J., Yu, H., & Zhang, L. 2017, *MNRAS*, 464, 940
 Fesen, R. A., Kwitter, K. B., & Downes, R. A. 1992, *AJ*, 104, 719
 Fesen, R. A., Weil, K. E., Cisneros, I., et al. 2021, *MNRAS*, 507, 244
 Fesen, R. A., Weil, K. E., Cisneros, I. A., et al. 2018, *MNRAS*, 481, 1786
 Ghavamian, P., Raymond, J., Smith, R. C., et al. 2001, *ApJ*, 547, 995
 Graham, J. R., Levenson, N. A., Hester, J. J., et al. 1995, *ApJ*, 444, 787
 Hartigan, P., Raymond, J., & Hartmann, L. 1987, *ApJ*, 316, 323
 Hester, J. J. 1987, *ApJ*, 314, 187
 Hester, J. J., & Cox, D. P. 1986, *ApJ*, 300, 675
 Hester, J. J., Parker, R. A. R., & Dufour, R. J. 1983, *ApJ*, 273, 219
 Hester, J. J., Raymond, J. C., & Blair, W. P. 1994, *ApJ*, 420, 721
 Joye, W. A., & Mandel, E. 2003, *ASPC*, 295, 489
 Katsuda, S., Maeda, K., Ohira, Y., et al. 2016, *ApJL*, 819, L32
 Klein, R. I., McKee, C. F., & Colella, P. 1994, *ApJ*, 420, 213
 Levenson, N. A., Graham, J. R., Aschenbach, B., et al. 1997, *ApJ*, 484, 304
 Levenson, N. A., Graham, J. R., Keller, L. D., et al. 1998, *ApJS*, 118, 541
 Levenson, N. A., Graham, J. R., & Snowden, S. L. 1999, *ApJ*, 526, 874
 Long, K. S., Blair, W. P., Vancura, O., et al. 1992, *ApJ*, 400, 214
 McKee, C. F., Hollenbach, D. J., Seab, G. C., et al. 1987, *ApJ*, 318, 674
 Medina, A. A., Raymond, J. C., Edgar, R. J., et al. 2014, *ApJ*, 791, 30
 Patnaude, D. J., Fesen, R. A., Raymond, J. C., et al. 2002, *AJ*, 124, 2118
 Raymond, J. C., Blair, W. P., Fesen, R. A., et al. 1983, *ApJ*, 275, 636
 Raymond, J. C., Chilingarian, I. V., Blair, W. P., et al. 2020a, *ApJ*, 894, 108
 Raymond, J. C., Edgar, R. J., Ghavamian, P., et al. 2015, *ApJ*, 805, 152
 Raymond, J. C., Hester, J. J., Cox, D., et al. 1988, *ApJ*, 324, 869
 Raymond, J. C., Slavin, J. D., Blair, W. P., et al. 2020b, *ApJ*, 903, 2
 Salvsen, G., Raymond, J. C., & Edgar, R. J. 2009, *ApJ*, 702, 327
 Sankrit, R., & Blair, W. P. 2002, *ApJ*, 565, 297
 Sankrit, R., Blair, W. P., Cheng, J. Y., et al. 2007, *AJ*, 133, 1383
 Sankrit, R., Blair, W. P., Raymond, J. C., et al. 2000, *AJ*, 120, 1925
 Sankrit, R., Raymond, J. C., Bautista, M., et al. 2014, *ApJ*, 787, 3
 Spangler, S. R. 2022, *RNAAS*, 6, 205
 Szentgyorgyi, A. H., Raymond, J. C., Hester, J. J., et al. 2000, *ApJ*, 529, 279